## Title

# Divergent antibody-enhanced entry across SARS-CoV-2 lineages drives variant-specific immunopathology through epistatically constrained spike evolution

## Authors

Yuru Han[1,†], Song Xue[1,†,*], Wei Xu[1,†], Yuanzhe Zhang[2,†], Xiaofang Peng[1,†], Yunjiao Zhou[3], Fei Wu[1,4], Minxiang Xie[1], Wei Wu[1], Anqi Xia[1], Yidan Gao[1], Jianbo Wu[5], Zezhong Liu[6], Jingsong Zhang[7], Shibo Jiang[1], Zhixiang Zuo[8,*], Fan Wu[1,*], and Qiao Wang[1,*]

## Affiliations

[1]Key Laboratory of Medical Molecular Virology (MOE/NHC/CAMS), Shanghai Institute of Infectious Disease and Biosecurity, Shanghai Frontiers Science Center of Pathogenic Microbes and Infection, School of Basic Medical Sciences, Shanghai Medical College, Fudan University, Shanghai 200032, China.

[2]Department of Radiology, State Key Laboratory of Oncology in South China, Guangdong Provincial Clinical Research Center for Cancer, Sun Yat-sen University Cancer Center, Guangzhou 510060, China.

[3]Fundamental Research Center, Shanghai Yangzhi Rehabilitation Hospital (Shanghai Sunshine Rehabilitation Center), School of Medicine, Tongji University, Shanghai 201619, China.

[4]Department of Epidemiology, School of Public Health, Fudan University, No.130 Dongan Road, Shanghai 200032, China.

[5]Department of Laboratory Medicine, Huashan Hospital, Shanghai Medical College,

Fudan University, Shanghai 200040, China.

[6]Department of Pharmacology & the Key Laboratory of Smart Drug Delivery Ministry of Education, School of Pharmacy, Fudan University, Shanghai 201210, China.

[7]Key Laboratory of Systems Biology, Shanghai Institute of Biochemistry and Cell Biology, Center for Excellence in Molecular Cell Science, Chinese Academy of Sciences, Shanghai 200031, China.

[8]State Key Laboratory of Oncology in South China, Guangdong Provincial Clinical Research Center for Cancer, Sun Yat-sen University Cancer Center, Guangzhou 510060, China.

[†]These authors contributed equally to this work.

[*]Correspondence: 17301010038@fudan.edu.cn (S.X.), zuozhx@sysucc.org.cn (Z.Z.), wufan@shmu.edu.cn (F.W.), wangqiao@fudan.edu.cn (Q.W.)

## Abstract

Antibody-dependent enhancement (ADE) of viral entry remains a mechanistically unresolved phenomenon in SARS-CoV-2 variants, with its variant-specificity and pathological consequences poorly defined. Through systematic profiling of 114 monoclonal antibodies (mAbs) across major variants of concern (VOCs), we discover that the Delta variant exhibits uniquely potent ADE mediated by mAbs targeting specific spike (S) epitopes. Crucially, integrative single-cell RNA sequencing of Delta-infected patients provides direct in vivo evidence of ADE-associated immunopathology, revealing significant depletion of $Fc\gamma R^+$ and $C1qR^+$ immune cells (particularly $CD16^+$ monocytes and dendritic cells) alongside pan-cellular cytokine hyperactivation, patterns that are absent in wildtype or Omicron infections. Functional dissection demonstrates epistatic interactions among Delta-specific S mutations (L452R, P681R, and D950N), wherein individual mutations enhance ADE in wildtype background but suppress it in Delta context. Longitudinal surveillance reveals fluctuating ADE patterns across variants, with BA.5 sub-lineage exhibiting L452R-mediated resurgence of enhancement. This study establishes variant-specific ADE as an in vivo driver of immunopathology governed by epistatic constraints, necessitating continuous risk assessment in evolving variants.

## Introduction

Antibody-dependent enhancement (ADE) is an immunological phenomenon in which monoclonal antibodies (mAbs), paradoxically, enhance viral infection rather than mediating neutralization. This occurs when the antigen-binding fragment (Fab) of a mAb binds to viral surface proteins on viral particles, while the fragment crystallizable (Fc) region interacts with Fc gamma receptors (FcγRs) expressed on immune cells, facilitating viral uptake (Supplementary Fig. S1a).[1,2] ADE of viral infection manifests through two primary consequences: elevated viral loads due to viral replication within FcγR$^+$ cells, and dysregulated immune activation resulting from excessive FcγR signaling within infected immune cells.[3,4] The ADE phenomenon has been documented for diverse viruses, including dengue virus (DENV), Zika virus (ZIKA), and respiratory syncytial virus (RSV), typically upon secondary exposure to homologous or antigenically related pathogens.

In the context of coronaviruses, studies have demonstrated FcγR-mediated uptake of SARS-CoV and MERS-CoV by human B lymphoblastoid cell line Raji cells (FcγRIIB$^+$), monocyte-derived macrophages (FcγRII$^+$), and exogenous FcγRIIA-expressing HEK293T cells in vitro in the presence of anti-spike (S) sera or mAbs.[5-7] establishing an in vitro "ADE of viral entry" phenotype for these viruses. Consequently, during the onset of the COVID-19 pandemic, the potential risk of ADE for SARS-CoV-2 represented a significant scientific concern.[4,8,9] Consistent with this, numerous in vitro studies, including our own, confirmed ADE of viral entry for wildtype (WT) SARS-CoV-2 induced by specific mAbs

interacting with FcγRs.[10-14] However, a critical discrepancy emerged between SARS-CoV-2 and other pathogenic coronaviruses. While active and passive immunization against SARS-CoV or MERS-CoV led to exacerbated immunopathology or heightened inflammatory responses upon infection in animal models,[15,16] passive transfer of SARS-CoV-2 mAbs, even those exhibited potent ADE in vitro, effectively protected mice and monkeys from high-dose SARS-CoV-2 challenge.[12] Furthermore, breakthrough infections among vaccinated individuals possessing anti-S antibodies have not been associated with exacerbated symptoms. Thus, direct evidence linking adverse clinical outcomes to an "ADE of disease" in vivo phenotype for SARS-CoV-2 is currently lacking.

As a single-stranded RNA virus, SARS-CoV-2 continuously undergoes mutations and recombination events, driving the emergence of distinct variants. Several notable variants exhibiting increased transmissibility, immune evasion capabilities and/or clinical severity have been designated variants of concerns (VOCs), including Alpha (B.1.1.7), Beta (B.1.351), Gamma (P.1), Delta (B.1.617.2), and Omicron (B.1.1.529) along with its numerous sub-lineages.[17] These VOCs underwent rigorous surveillance due to their significant public health implications. Extensive research focused on the dynamic evolution of their S proteins, particularly concerning alteration in binding affinity to the host receptor angiotensin-converting enzyme 2 (ACE2) and enhanced antibody evasion capacity, factors critically influencing viral fitness.[18-20] However, whether these VOCs exhibit comparable or altered ADE potential relative to the ancestral wildtype SARS-CoV-

2 remained largely unexplored.

In this study, we systematically evaluated in vitro ADE of viral entry across SARS-CoV-2 variants. Our results revealed that the Delta variant exhibits significantly enhanced ADE capacity in an epitope-associated manner. Integrated single-cell RNA sequencing (scRNA-seq) analysis of human peripheral blood mononuclear cells (PBMCs) from Delta-infected patients indicated a significant depletion of immune cell subsets expressing FcγRs or complement component C1q receptors (C1qRs), accompanied by a universal upregulated of cytokine gene expression. Further dissection of the specific combination of mutations within the Delta S protein demonstrated profound epistatic effects on ADE of viral entry. Finally, fluctuating patterns of ADE potential (induced by both mAbs and donors' sera) across major SARS-CoV-2 variants over time, with more robust ADE for the Delta and Omicron BA.5, revealed the stochastic emergence of ADE-strong variants, emphasizing the critical need for continuous ADE surveillance.

## Methods

### Cell lines

HEK293T cells (human embryonic kidney epithelia cell line) and Huh-7 cells (human hepatocellular carcinoma cell line) were maintained in Dulbecco's Modified Eagle Medium (DMEM) (MeilunBio) supplemented with 10% fetal bovine serum (FBS, Deary Tech), 100 U/mL penicillin, and 100 μg/mL streptomycin. Raji cells (human Burkitt's lymphoma B lymphoblast) were cultured in RPMI1640 medium (MeilunBio) containing 10% FBS under identical condition. HEK293F cells were adapted to serum-free suspension culture in OPM-293-CD05 medium (OPM Biosciences) with orbital shaking at 100 rpm. All cell lines were cultured at 37℃ under 5% $CO_2$.

### Antibody cloning and production

Human mAbs were cloned and produced as previously reported.[10] Briefly, heavy chain and light chain expression plasmids were co-transfected into HEK293F suspension cells at a 1:1 ratio using EZtrans transfection reagents (Life iLAB Bio-Technology). Cell supernatants were harvested seven days post-transfection, and antibodies were purified using Protein G Sepharose 4 Fast Flow (Cytiva). Purified antibodies were analyzed by SDS-PAGE under reducing conditions, confirming expected molecular weight (~50 kDa for heavy chains; ~25 kDa for light chains). Final antibody preparation was buffer-exchanged into PBS (pH 7·4), filtered (0·22 μm), and stored at 4°C until use.

### Generation of pseudotyped viruses

Pseudotyped viruses bearing SARS-CoV-2 spike (S) proteins were generated as previously

described.[21,22] Briefly, wildtype, variant-specific, and mutant S protein sequences were cloned into the pcDNA3.1 vector for mammalian expression. HEK239T cells were transiently co-transfected with the pNL4-3.Luc.R-E- backbone plasmid and S protein-expressing plasmids at a 1:2 ratio using VigoFect transfection reagent (Vigorous Biotechnology). Six hours post-transfection, supernatants were replaced with fresh complete DMEM supplemented with 10% FBS. Pseudovirus-containing supernatants were harvested 48 hours later, aliquoted, and stored at -80℃. To generate SARS-CoV-2 pseudoviruses containing mutated S protein, site-directed mutagenesis was performed using the mut Express II Fast Mutagenesis Kit V2 (Vazyme) with pcDNA3.1-SARS-CoV-2-wildtype-S or -Delta-S as template. Pseudovirus quantification was performed by quantitative reverse transcription PCR (qRT-PCR). Briefly, viral RNA was extracted using TIANamp virus RNA kit (TIANGEN), reverse transcribed with HiScript® II Q RT SuperMix (Vazyme), and amplified using Taq Pro Universal SYBR qPCR Master Mix (Vazyme) with primers targeting gag, pol, and luciferase genes in the pNL4-3.Luc.R-E- backbone. All pseudovirus stocks were normalized to $2\times10^4$ copies/μL prior to use in ADE assay.

**In vitro ADE assay using pseudoviruses**

In vitro ADE of viral entry was assessed using Raji cells in a standardized pseudovirus assay as previously established.[5,10] Briefly, Raji cells were seeded at $3\times10^4$ cells/well in poly-L-lysine-coated (0·01%) 96-well plates and cultured for 24 hours. Pseudoviruses were incubated with serially diluted mAbs (nine-point three-fold dilutions starting from 100 μg/mL) or sera (nine-point three-fold dilutions starting from 1:4 dilution) for 30 minutes at

37°C. The virus-antibody mixtures were then added to Raji cells and incubated for 60 hours. Luciferase activity was quantified using the Firefly Luciferase Assay Kit (Promega) according to manufacturer specifications. Since many factors (cell concentration, immunofluorescence reading, etc.) varied in distinct plates or different rounds of experiments, we normalized results across experimental plates and batches. Specifically, antibody XG043[10] (2 μg/mL) against wildtype SARS-CoV-2 was included in triplicate on each plate as an internal reference standard. Absolute luciferase reading values from all wells were converted to relative percentages by setting the average value of XG043 replicates to 100%.

**In vitro ADE assay using authentic viruses**

In vitro Raji cell-dependent ADE assays with authentic SARS-CoV-2 viruses, including wildtype, Delta, and Omicron strains, were conducted in a Biosafety Level 3 (BSL-3) laboratory. All personnel wore appropriate personal protective equipment (PPE) including powered air-purifying respirators (PAPRs) during BSL-3 procedures. Prior to infection, viral inocula were normalized to equivalent RNA copy numbers via qRT-PCR. Antibodies were used at 10 μg/mL or serially diluted (six-point three-fold dilutions; maximum concentration 90 μg/mL) in serum-free RPMI1640 medium (MeilunBio). Seeded Raji cells were incubated with virus-antibody mixtures. Following 24-hour incubation, cells were lysed using Trizol LS reagent (Thermo Fisher Scientific) and total RNA was extracted as described previously.[23] Viral RNA quantification was performed via one step qRT-PCR using the One-Step Prime Script RT-PCR kit (Takara Bio) following the manufacturer's instructions. Primers targeting the SARS-CoV-2 nucleocapsid (N) gene were used for qRT-

PCR.

**In vitro neutralization assay using pseudoviruses**

In vitro pseudovirus neutralization assays were performed as previously described.[21,24,25] Briefly, Huh-7 cells were seeded at $1\times10^4$ cells/well in 96-well plates using complete DMEM and cultured for 8 hours. Serial dilutions of mAbs (nine-point three-fold dilutions starting from 10 μg/mL) or sera (nine-point two-fold dilutions starting from 1:40 dilution) were incubated with pseudoviruses for 30 minutes at 37℃ before transfer to seeded Huh-7 cells. Following 24-hour incubation, medium was replaced with fresh complete DMEM. Cells were harvested 36 hours post-infection and lysed for luciferase activity quantification using the Firefly Luciferase Assay Kit (Promega) according to the manufacturer's instructions. Neutralization curves were generated in GraphPad Prism, with $IC_{50}$ and $NT_{50}$ values calculated for mAbs and sera, respectively, using nonlinear regression analysis of GraphPad PRISM.

**Bulk RNA sequencing analysis**

Raw RNA sequencing reads underwent quality control assessment using FastQC (v0.11.9). Adapter trimming and quality filtering were performed using fastp (v0.23.2), and the final quality metrics were aggregated using MultiQC (v1.18). To deplete ribosomal RNA (rRNA), reads were aligned to an rRNA reference using HISAT2 (v2.2.1) and concordantly aligned reads were removed. The remaining clean reads were subsequently aligned to the GRCh38 human reference genome together with SARS-CoV-2 (MN996528.1) reference genome using the STAR aligner (v2.7.10). Resulting alignments were converted, sorted,

and indexed using Samtools (v1.10), generating sorted BAM files. Gene-level expression was quantified using featureCounts (v2.0.3) against the GENCODE v37 gene annotation, yielding a raw count matrix. For downstream analysis, gene counts were normalized to Transcripts Per Million (TPM) to account for sequencing depth and gene length. To visualize the global expression patterns and assess clustering among virus-infected sample groups, Principal Component Analysis (PCA) was performed on the log2-transformed TPM values (log2(TPM+1)). Separately, the raw count matrix was used for differential expression analysis with the DESeq2 R package (1.46.0).

**Single-cell RNA sequencing (scRNA-seq) data analysis**

To enable comparative analysis of immune cell populations and transcriptomic profiles across SARS-CoV-2 variants, we integrated scRNA-seq datasets from two independent studies. Processed Seurat objects containing original scRNA-seq datasets were obtained directly from the original publication.[26] Raw sequencing data for Omicron-infected cohort (accession ID HRA003738[27]) were retrieved from the China National Center for Bioinformation. Raw sequencing files were then aligned to the GRCh38 human reference genome using Cell Ranger (v8.0.0). Downstream data integration and analysis was performed in R package Seurat (v5.1.0) and the Python package Scanpy (v1.10.1). Quality control filtering excluded: (i) cells with less than 500 UMI counts, (ii) cells expressing less than 200 genes, and (iii) cells with more than 10% mitochondrial gene content. Potential doublets identified by DoubletFinder (v2.0.4) with default parameters were also excluded. Gene expression normalization was performed and top 2000 most variable features were selected for subsequent dimensionality reduction. Principal component analysis (PCA) was

227 performed for dimensionality reduction, UMAP algorithm was then implemented for two-
228 dimensional visualization. To integrate cells from different datasets and perform batch
229 effect correction, the BBKNN algorithm was employed. Cell clustering was performed on
230 the batch-corrected neighbor graph generated by BBKNN with the *sc.pl.leiden* function
231 from Scanpy. Cell type annotation was conducted through systematic evaluation of
232 canonical marker genes and expression profiles. Following manual curation and cross-
233 validation with reference datasets, a total of 709,493 high-quality single cells were
234 annotated across 12 distinct immune populations: $CD8^+$ T cells (140,048), $CD4^+$ T cells
235 (212,464), $CD16^+$ monocytes (10,141), $CD14^+$ monocytes (157,509), B cells (78,665),
236 cDCs (1,808), pDCs (1,059), erythroblasts (2,223), neutrophils (612), NK cells (86044),
237 plasma cells (1,693), and platelets (17,227).
238
239 **Expression analysis of FcγR and C1qR**
240 The expression profiles of genes encoding FcγRs (FCGR1A, FCGR2A, FCGR2B, and
241 FCGR3A) and C1q receptors (C1QBP and CD93) were extracted from scRNA-seq datasets
242 using the *GetAssayData function* in Seurat. Normalized expression values were analyzed
243 among annotated cell types for comparative analysis.
244
245 **Cytokine scoring**
246 A curated panel of cytokine genes (Supplementary Table S3) obtained from a previous
247 study[28] was used to compute cell-level cytokine scores via the *AddModuleScore* function
248 in Seurat. Scores represent the average normalized expression of cytokine genes relative to
249 control gene sets.

## Statistical analysis

Statistical analyses were performed as detailed in Results and figure legends. ADE AUC values were calculated using GraphPad PRISM. Normality was assessed using Shapiro-Wilk test. For normally distributed data, Brown-Forsythe and Welch's ANOVA test and Dunnett's multiple comparisons test were performed. For non-normal distributions, Kruskal-Wallis test with Dunnett's multiple comparisons was applied. All tests used two-sided thresholds with significance defined as $p < 0{\cdot}05$.

## Ethics

All participants initially provided oral informed consent, followed by written informed consent. This study was conducted according to the guidelines of the Declaration of Helsinki and was approved by the Fudan University School of Basic Medical Sciences Ethics Committee (FUSBMSEC) (2022-C005).

## Role of funders

None of the funding sources had any role in study design, data analysis, preparation of manuscript or decision to submit the manuscript for publication.

## Results

### Distinct ADE patterns across SARS-CoV-2 variants and mAbs

To accurately characterize the capacity for ADE of viral entry in vitro, we employed our established ADE assay (Supplementary Fig. S1b). This assay utilized Raji cells expressing FcγRIIB but lacking ACE2 expression, thereby preventing infection via the conventional S-ACE2-dependent viral entry pathway.[5] SARS-CoV-2-pseudotyped viruses encoding a luciferase reporter gene were used. Consequently, the efficiency of FcγR-mediated viral entry into Raji cells was quantified by measuring luciferase activity.

We next assembled a panel of human mAbs targeting diverse epitopes on the SARS-CoV-2 S protein, comprising: 76 mAbs isolated from one convalescent individual (XG series) and four vaccinated individuals (XGv series) in our prior studies.[10,29] and 38 structurally characterized mAbs compiled from published literatures (Supplementary Table S1). This combined, unbiased panel enabled systematic profiling of ADE activity against the wildtype SARS-CoV-2 strain and major VOCs, including Alpha, Beta, Gamma, Delta, and Omicron. The ADE potency of each mAb against each variant was evaluated across a broad concentration gradient (100 to 0·015 μg/mL) using nine serial three-fold dilutions (Fig. 1a).

Based on the luciferase reporter activities elicited, the 114 mAbs exhibited divergent ADE capacities across SARS-CoV-2 variants (Fig. 1a). To quantify differences in ADE capacity among these mAbs across variants, we employed two key metrics: the ADE area under

curve (ADE AUC) and ADE enhancing power (defined as the maximum luciferase signal achieved across antibody dilutions) (Supplementary Fig. S2a). Correlation analyses revealed strong positive associations between ADE AUC and enhancing power for each variant ($p < 0{\cdot}001$; Supplementary Fig. S2b-g), validating the use of these quantitative parameters for assessing ADE potency.

Several key phenomena were observed across the tested VOCs and mAbs. First, a large proportion of mAbs did not induce substantial ADE, aligning with prior studies on the wildtype virus (Fig. 1a).[10] Uniform manifold approximation and projection (UMAP) dimensional reduction of ADE AUC profiles clearly delineated three distinct clusters among these mAbs (Fig. 1b). We designated these clusters as high, moderate and low ADE based on their overall ADE AUC values. Over half of mAbs (66 out of 114) belonged to the low ADE cluster, failing to promote enhancement of viral entry at any tested mAb concentrations across all kinds of variants tested.

Second, the ADE capacity of mAbs strongly correlated with epitope specificity, consistent with our previous findings.[10,30] Antibodies within the high or moderate ADE clusters were predominantly specific for particular epitopes, including receptor-binding domain (RBD) class II/III and N-terminal domain (NTD) (Fig. 1c). Notably, 7 of 17 RBD class II (41·2%), 15 of 19 RBD class III (78·9%), and 22 of 37 NTD (59·5%) mAbs belonged to the high or moderate ADE clusters, while few of such mAbs (≤ 20%) were identified among RBD

class I/IV and S2 mAbs (Fig. 1c).

Third, the optimal mAb concentrations for inducing maximal ADE varied by epitope specificity, which was also observed in our previous studies.[10,30] For example, ADE-positive NTD-targeting mAbs exhibited enhancement predominantly at higher concentrations (Fig. 1a). Conversely, RBD class III mAbs typically induced potent ADE across a broad concentration range, while optimal concentrations for RBD class II mAbs were more variable (Fig. 1a).

Fourth, importantly, ADE-positive mAbs targeting RBD class II/III and NTD induced significantly more profound ADE effect against the Delta variant (Fig. 1a), as reflected by their significantly higher ADE AUC values and elevated enhancing power compared with wildtype and other VOCs (Supplementary Fig. S3a and b).

Collectively, anti-S mAbs targeting distinct epitopes across the SARS-CoV-2 S protein exhibited markedly divergent capacities for mediating ADE of viral entry in an epitope-associated manner, with the Delta variant eliciting uniquely potent ADE activity relative to the wildtype strain and other VOCs tested.

**Delta variant elicits the most potent ADE of viral entry in vitro**

Comparative analysis of ADE profiles across SARS-CoV-2 variants revealed statistically

significant elevations in both ADE AUC and enhancing power for the Delta variant, but not for other VOCs, relative to wildtype SARS-CoV-2 ($p < 0{\cdot}001$; Fig. 1d and e). Moreover, the ADE AUC and enhancing power elicited by the Delta variant were statistically higher than all other tested VOCs ($p < 0{\cdot}001$; Supplementary Fig. S3c and d). In contrast, the Omicron variant displayed weak ADE activity comparable to wildtype SARS-CoV-2 ($p > 0{\cdot}05$; Fig. 1d and e).

To investigate whether diverse ADE capacities for distinct variants result from alterations in mAbs' binding or neutralizing activity, we measured the $EC_{50}$ (binding) and $IC_{50}$ (neutralizing) values across the mAb panel (Fig. 1f, and Supplementary Table S2). Representative mAbs, such as XG003 and XG013, potently neutralized wildtype and VOCs, except Omicron, but induced considerable ADE only against Delta (Fig. 1g). Conversely, mAbs, such as XG005, LY-CoV1404, XGv282, and XGv289, maintained potent neutralizing activity ($IC_{50} < 0{\cdot}1$ μg/mL) against all tested variants, including Omicron, but also induced substantial ADE only with Delta (Fig. 1h and Supplementary Fig. S3e). Neither linear regression analysis nor principal component analysis (PCA) revealed significant correlations between ADE AUC and $IC_{50}$ values across variants (Fig. 1i and Supplementary Fig. S3f).

Collectively, our findings suggested that the pronounced ADE heterogeneity across major SARS-CoV-2 variants, particularly the enhanced ADE of Delta, is not attributable to

352 changes in mAb neutralization efficiency, but is likely to be driven by variant-specific
353 mutational profiles within the viral S protein.
354
355 **Authentic virus assays confirm potent ADE-mediated viral entry for Delta**
356 To validate the enhanced ADE capacity of the Delta variant observed in the pseudovirus
357 system, we performed analogous assays using authentic SARS-CoV-2 viruses, including
358 wildtype, Delta, and Omicron strains. We selected anti-RBD mAb XG005[21] due to its
359 consistently potent neutralizing activity against the tested VOCs (Fig. 1h). Mixtures of
360 XG005 and authentic viruses were incubated with Raji cells, and viral entry efficiency was
361 quantified by measuring intracellular viral RNA copy numbers via quantitative real-time
362 polymerase chain reaction (qRT-PCR). Three viral loads ($1{\cdot}50\times10^5$, $7{\cdot}50\times10^4$, and
363 $3{\cdot}75\times10^4$ RNA copies/μL) were tested. Consistent with findings in pseudovirus, Delta-
364 infected groups exhibited significantly elevated viral RNA levels in the presence of 10
365 μg/mL ADE-positive antibody XG005, exceeding both wildtype and Omicron groups by
366 3~9-fold ($p < 0{\cdot}001$; Fig. 2a).
367
368 We then evaluated ADE capacity using serially diluted XG005 mAb (90 to 0·37 μg/mL)
369 with a standardized viral load ($1{\cdot}50\times10^5$ RNA copies/μL) selected for optimal ADE
370 discrimination. Across all tested XG005 concentrations, Delta variant consistently
371 exhibited the highest entry efficiency, with > 5-fold increase compared with wildtype and
372 Omicron (Fig. 2b). In contrast, none of the variants showed enhanced entry with ADE-

373 negative anti-S2 antibody hr2.016 (Fig. 2c).[31]

374

375 To further confirm ADE-mediated entry of authentic Delta virus, we performed bulk RNA
376 sequencing of Raji cells from ADE assays. Consistent with the qRT-PCR results, Delta-
377 infected cells treated with XG005 exhibited significantly higher viral genome levels than
378 Omicron-infected counterparts ($p < 0{\cdot}001$; Fig. 2d). Complete abrogation of ADE activity
379 was observed in both Delta and Omicron groups treated with the ADE-negative mAb
380 hr2.016 or the FcγR-binding deficient mutant mAb XG005-GRLR (containing
381 G236R/L328R mutations in Fc).[10]

382

383 We extended this analysis to additional mAbs selected based on epitope profiles. Similar
384 to XG005, mAbs 1-87 and LY-CoV1404 enhanced viral entry across all three variants, with
385 Delta-infected groups showing significantly higher intracellular viral RNA copies than
386 wildtype or Omicron groups (Fig. 2e). Antibody 5-7 selectively promoted cellular entry of
387 Delta with minimal effect on wildtype or Omicron (Fig. 2e). All ADE-negative mAbs
388 showed markedly reduced or absent entry enhancement, mirroring the pattern observed
389 with XG005-GRLR.

390

391 Taken together, in vitro ADE assays using authentic virus confirmed that the Delta variant
392 exhibits uniquely potent ADE-mediated viral entry when exposed to ADE-positive
393 antibodies.

**In vivo depletion of FcγRs- and C1qRs-expressing cells in Delta-infected patients**

Given the significantly enhanced ADE of viral entry observed for the Delta variant in vitro using both pseudovirus and authentic virus systems, we sought to determine whether this effect manifests in vivo through alterations in immune cell populations or transcriptional programs. We performed an integrative analysis of publicly available scRNA-seq datasets from PBMCs of patients infected with SARS-CoV-2 wildtype, Delta or Omicron,[26,27] alongside healthy individual controls. After rigorous quality control and batch correction, 709,493 high-quality single cells from 48 wildtype-infected, 9 Delta-infected, 19 Omicron-infected patients, and 14 healthy individuals were analyzed (Fig. 3a). Unsupervised UMAP analysis based on canonical cell markers identified 12 major immune populations, encompassing the diversity of peripheral blood lineages (Fig. 3a, and Supplementary Fig. S4a-c).

Considering the established role of FcγRs in mediating ADE in vitro, we first assessed the expression of genes encoding major human FcγR subtypes, including FCGR1A (FcγRI), FCGR2A (FcγRIIA), FCGR2B (FcγRIIB), and FCGR3A (FcγRIIIA) genes. The proportion of FcγR-positive cells (expressing at least one FCGR gene) (Fig. 3a) was significantly increased in both wildtype- and Omicron-infected patients compared with healthy controls (Fig. 3b). However, importantly, Delta-infected patients exhibited significant decreases in FcγR-positive cell frequency relative to both wildtype- and Omicron-infected patients (Fig.

3b). This suggested that, unlike wildtype and Omicron infection, Delta infection fails to have higher levels of peripheral FcγR-expressing immune cells, indicating variant-specific impairment in the recruitment or maintenance of these populations.

To pinpoint the specific FcγR subtypes underlying this global reduction in $FcγR^+$ cells in Delta infection, we performed subtype-specific analysis. The proportion of $FCGR1A^+$ cells (predominantly $CD14^+$ monocytes and $CD16^+$ monocytes) was significantly depleted in Delta-infected individuals compared with both wildtype- ($p < 0.001$) and Omicron-infected ($p = 0{\cdot}007$) groups (Fig. 3c). Conversely, the frequency of $FCGR2A^+$ cells expanded significantly across all infected cohorts relative to healthy controls ($p < 0{\cdot}05$), with no significant differences ($p > 0{\cdot}05$) observed among variant groups (Fig. 3d). Given the predominant expression of FCGR2B in B cells and its documented role in mediating ADE in vitro, we analyzed its expression pattern. Substantial depletion of $FCGR2B^+$ cells was observed in Delta-infected patients compared with the wildtype-infected group ($p = 0{\cdot}002$); however, frequencies were comparable between Delta and Omicron cohorts (Fig. 3e). Moreover, the frequency of $FCGR3A^+$ cells significantly lower in the Delta cohort relative to wildtype, Omicron, and healthy control groups (Fig. 3f). Together, these findings identified FCGR1A and FCGR3A as primary contributors to the diminished $FcγRs^+$ compartment during Delta infection, highlighting complex variant-specific immunomodulation in vivo.

We next analyzed the compositional changes in broad immune cell categories to identify populations most and uniquely affected by Delta infection. $CD16^+$ monocytes, which express multiple FCGR genes, exhibited significant depletion in Delta-infected patients compared with wildtype- ($p < 0{\cdot}001$), Omicron- ($p < 0{\cdot}001$) infected individuals and healthy controls ($p = 0{\cdot}004$) (Fig. 3g). In contrast, frequencies of other FcγR-expressing cells, including $CD14^+$ monocytes, NK cells and B cells, showed no substantial differences across cohorts (Fig. 3g). Minimal alterations were also observed in $CD4^+$ T and $CD8^+$ T cells, consistent with their low FcγR expression (Fig. 3g). Thus, these findings identified $CD16^+$ monocytes as the most significantly altered population in Delta infection, implying potential FcγR-mediated pathophysiology specific to this variant.

Unexpectedly, significant depletion was also observed for both conventional dendritic cells (cDCs) and plasmacytoid dendritic cells (pDCs) uniquely in the Delta cohort (Fig. 3g), despite the lack of dominant FcγR expression in these two cell types. This prompted investigation into alternative antibody-dependent mechanisms. Beyond FcγRs, the classical complement pathway, activated via C1q binding to antibody Fc regions, can also facilitate viral entry.[8,32] Critically, C1q-mediated ADE of viral entry has been experimentally demonstrated for wildtype SARS-CoV-2 in vitro.[33] We therefore mapped expression profiles of key C1q receptors, C1QBP and CD93, across immune cell subsets using scRNA-seq. Both cDCs and pDCs exhibited uniquely elevated expression of these receptors, particularly C1QBP (Fig. 3h). Quantification of both $C1QBP^+$ and $CD93^+$ cells

457 confirmed significantly reduced frequencies specifically in the Delta cohort relative to
458 other groups (Fig. 3i and j). Thus, these consistent patterns suggested that receptor
459 expression levels, rather than cellular identity, predispose cells to depletion during Delta
460 infection, potentially implicating C1q-mediated pathways in parallel to FcγR-mediated
461 mechanisms in Delta-specific pathogenesis.
462
463 To assess functional consequences of these cellular alterations, we quantified cytokine
464 production using a cell-level cytokine score based on a curated panel of genes
465 (Supplementary Table S3).[28] Delta-infected patients exhibited universally elevated
466 cytokine scores across cell types (Fig. 3k, l, and Supplementary Fig. S4d), indicating
467 systemic immune activation consistent with a cytokine storm phenotype. Notably, platelets
468 also demonstrated significant cytokine gene upregulation (Fig. 3k), aligning with reported
469 functional alterations of platelets in SARS-CoV-2 infection.[34,35]
470
471 **Point mutations for ADE in an epistatic manner**
472 Given the extraordinary ADE capacity of the Delta variant, we sought to identify specific
473 amino acid mutations on Delta S protein responsible for ADE enhancement. Compared
474 with both wildtype SARS-CoV-2 and other four VOCs, Delta possesses several unique
475 point mutations in its S protein, including T19R, G142D, EFR156-158G, L452R, T478K,
476 P681R and D950N (Fig. 4a). We generated pseudoviruses containing each of these
477 mutations using the wildtype S protein backbone and assessed their ADE activity by our in

vitro assay with ADE-positive and ADE-negative mAbs targeting distinct epitopes.

All ADE-negative mAbs failed to induce ADE across all constructed mutants (Fig. 4b). However, ADE-positive mAbs elicited elevated ADE effects at varying antibody concentrations with specific mutants (Supplementary Fig. S5a). Three key mutations, L452R, P681R and D950N, introduced individually into the wildtype backbone enhanced ADE ubiquitously for ADE-positive mAbs (Fig. 4b and Supplementary Fig. S5b). Specifically, the wildtype-L452R mutant, compared with wildtype, exhibited an enhanced viral entry (up to 9·19-fold) with all ADE-positive mAbs (Fig. 4b); the wildtype-P681R mutant showed 2·25- to 5·70-fold increased ADE activity with half of the ADE-positive mAbs (Fig. 4b); and the WT-D950N mutant demonstrated an enhancement pattern similar to wildtype-L452R, with mAb 5-7 showing a 16-fold increase (Fig. 4b). Notably, the ADE levels observed with single mutants were substantially lower than the Delta variant harboring all tested mutations simultaneously, indicating synergistic ADE effect (Fig. 4b). Moreover, among these three mutations, only L452R exhibited direct interactions with specific RBD class II/III mAbs, indicating that the ADE modulation stems from global S protein functional alterations, rather than direct S-mAb interactions.

Pseudoviruses containing other Delta-specific mutations generally showed reduced or even abolished viral entry with ADE-positive mAbs, further emphasizing the importance of three Delta-specific mutations, L452R, P681R, and D950N. However, surprisingly,

reverting mutants (R452L, R681P and N950D) in the Delta backbone significantly enhanced, but not suppressed, ADE of viral entry even beyond the Delta variant with most ADE-positive mAbs (Fig. 4c, and Supplementary Fig. S5c and d). These results suggested that L452R, P681R, and D950N individual mutations enhanced ADE in the wildtype S protein backbone, but strongly inhibited ADE in the Delta S protein backbone, a hallmark epistatic phenomenon reflexing complex interactions among S protein residues.

Given the significant impact of these three mutations on ADE, we tracked their epidemiological persistence using global SARS-CoV-2 sequencing data from GISAID (Fig. 4d). D950N, located in the heptad repeat 1 (HR1) of S2 region, was exclusive to Delta and absent in subsequent variants. L452R, located in RBD, showed sustained prevalence: initially in B.1.427/B.1.429 lineages, then in Delta (mid 2021), and later in BA.4/5, CH.1.1, and HV.1 variants. Similarly, P681R, within S1/S2 cleavage site, re-emerged in BA.2.86 and JN.1 variants.

We then evaluated ADE activity in strains harboring these mutations alongside circulating variants. Most Omicron sub-lineages exhibited very low levels of ADE activity with ADE-positive mAbs, with BA.2 showing ADE levels similar to Omicron variant (Fig. 4e, and Supplementary Fig. S5e). Uniquely, BA.5, harboring L452R, displayed strengthened ADE across antibody concentrations (Fig. 4e, and Supplementary Fig. S5e). Especially, the ADE-negative mAb SA58 unexpectedly induced considerable ADE with BA.5, suggesting

the unique ADE-inducing capability of this variant. Reversely introducing R452L into BA.5 largely impaired its ADE activity (Supplementary Fig. S5e and f). Moreover, other L452R-harboring variants such as CH.1.1 and HV.1 exhibited minimal ADE effect (Fig. 4e, and Supplementary Fig. S5e), possibly due to the diminished or loss of neutralizing efficiency of the tested mAbs (Supplementary Table S2) induced by viral immune evasion.

In summary, functional dissection of S protein mutations revealed complex epistatic interactions within the viral S protein.

**Fluctuating patterns of serological ADE across SARS-CoV-2 variants**

To investigate the serological ADE of viral entry across distinct SARS-CoV-2 variants, we evaluated ADE capacity using sera from 46 donors vaccinated or recovered from BA.5 infection (Supplementary Table S4). These sera exhibited potent neutralization against wildtype and nine tested variants (Supplementary Fig. S6), confirming sufficient antibody binding capacity. Consistent with prior reports,[10,30] almost all sera failed to induce substantial viral entry enhancement for wildtype SARS-CoV-2 (Fig. 5a and b). This limited enhancement profile was similarly observed for Alpha, Omicron, and BA.1 variants (Fig. 5, a and b). In contrast, Beta, Gamma, BA.2 and BA.3 variants displayed elevated ADE in multiple serum samples, while both Delta and BA.5 variants exhibited the most potent ADE, with 7·01-fold ($p < 0·001$) and 2·82-fold ($p < 0·001$) increases in entry efficiency relative to wildtype (Fig. 5a and b). No significant correlations were observed between serological

ADE levels and donors' characteristics, including the number of prior SARS-CoV-2 infections, volunteers' age, body mass index (BMI), and gender (Supplementary Fig. S7). However, as time elapsed, serological ADE decreased along with reduced antibody titers (Supplementary Fig. S7e). These findings indicated that the serum samples could drive ADE of viral entry against susceptible variants, particularly Delta and BA.5.

Collectively, the fluctuating serological ADE patterns across SARS-CoV-2 variants mirrored those observed with mAbs, suggesting conserved FcγR engagement mechanisms driving viral internalization in vivo for variants with enhanced ADE capacity, notably Delta and BA.5. These findings also underscored concerns that newly emerged variants may unpredictably acquire potent ADE capabilities, potentially triggering subsequent pandemic waves.

## Discussion

While current understanding of ADE in SARS-CoV-2 has primarily focused on the wildtype virus, our systematic characterization across major SARS-CoV-2 variants of concern (VOCs) revealed profound variant-specific differences. Our results showed that the Delta variant exhibits significantly enhanced ADE of viral entry compared with other VOCs, a finding consistent across pseudovirus- and authentic virus-based in vitro assays. This distinctive phenotype may constitute a previously unrecognized mechanism underlying the clinical severity associated with Delta infections,[36-38] complementing

562 Delta's established capacities for enhanced replication, elevated S-mediated cell-cell fusion,
563 and immune evasion.[39,40]

564

565 So far, ADE of disease in vivo has not been well documented. This discordance between
566 in vitro ADE observations and in vivo outcomes might be attributed to abortive viral
567 replication in target immune cells following FcγR-mediated entry.[5,6,10,41] However, our
568 integrated single-cell analysis revealed critical pathophysiological insights: significant
569 depletion of $FcγR^+$ (such as $FcγRIIIA^+$-expressing $CD16^+$ monocytes) and $C1qR^+$ (such as
570 cDCs and pDCs) cells coupled with pan-cellular cytokine hyperactivation in Delta-infected
571 patients, but not in wildtype- and Omicron-infected individuals. These findings suggest
572 that ADE-mediated viral entry, even without productive replication, could trigger
573 inflammatory cascades leading to proinflammatory cell death, such as pyroptosis, and
574 hyperactivation of proinflammatory signaling. This aligns with previous reports of
575 complement hyperactivation in COVID-19 patients[42] and monocyte pyroptosis triggered
576 by wildtype SARS-CoV-2,[41,43] positioning ADE as a potential amplifier of COVID-19
577 immunopathology.[44]

578

579 Epistasis is a pervasive phenomenon, in which one mutation influences the phenotypic
580 effects of other mutations by direct and indirect physical interactions, resulting in a non-
581 additive impact on the protein's physical properties, such as conformation, stability, or
582 affinity to antigens.[19] Here, we identified profound epistatic effects among Delta signature

583 mutations, including L452R, P681R, and D950N. While individually enhancing ADE in a
584 wildtype background, these Delta mutations paradoxically suppressed ADE when
585 introduced into the Delta backbone, mirroring epistasis patterns observed in ACE2 affinity
586 for the N501Y and Q498R substitutions.[45,46] This non-additive mutational interplay
587 underscores the contextual nature of viral fitness determinants and highlights ADE as an
588 underappreciated dimension of SARS-CoV-2 evolution.
589
590 ADE-enhancing mutations could be either variant-specific, such as D950N in the Delta, or
591 persistent in circulating variants, which raises significant concerns. For example, the
592 L452R mutation, recurrently emerging in Delta, BA.5, and subsequent Omicron sub-
593 lineages, confers both immune evasion and enhanced ADE of viral entry. This dual
594 functionality exemplifies how single mutations can simultaneously enhance
595 transmissibility, pathogenesis, and antibody evasion. Our findings underscore the
596 imperative for integrated surveillance of ADE potential against newly emerging variants,
597 alongside conventional metrics of immune escape and transmissibility.
598
599 Lastly, epitope specificity emerged as a critical determinant of ADE capacity, with
600 antibodies targeting RBD class II/III and NTD showing potent enhancement. These mAbs
601 engage SARS-CoV-2 S protein in both “down” (closed) and “up” (ACE2-accessible)
602 conformations, supporting that bivalent binding facilitates ADE of viral entry.[11] Moreover,
603 during the ADE process, the internalized antibody-virus complex enters host endosomes

via FcγRs, undergoes endosomal acidification, and triggers S conformational changes that enable membrane fusion. The pH-dependent binding affinity observed for ADE-positive anti-DENV mAbs[47] further implied that S conformational dynamics during endosomal entry may similarly influence SARS-CoV-2 ADE, warranting further investigation.

In summary, this study establishes ADE of viral entry as a variant-dependent phenomenon with profound implications for SARS-CoV-2 pathogenesis and evolution. The epistatic interactions governing ADE highlight the unpredictability of viral adaptation, necessitating ongoing assessment of emerging variants' capacity to exploit antibody-dependent entry pathways.

## Contributors

Conceptualization, Q.W. and F.W.; investigation, Y.H., S.X., W.X., Y.Z., X.P., Y.Z., F.W., M.X., W.W., A.X., Y.G., J.W., Z.L., J.Z., S.J., Z.Z., F.W., and Q.W.; software, Y.H., S.X., and Y.Z.; writing-original draft, Y.H., and S.X.; writing-review and editing, Y.H., S.X., and Q.W.; supervision, Z.Z., F.W., and Q.W.; All authors have read and agreed to the published version of the manuscript.

## Data sharing statement

The raw sequencing data of in vitro ADE assay using authentic viruses in this study have been deposited in the Genome Sequence Archive in National Genomics Data Center under the accession number HRA013827. All data and code used for this study will be available upon request.

## Declaration of Interests

The authors have declared that no conflict of interest exists.

## Acknowledgments

We gratefully acknowledge all data contributors and their original laboratories for generating the sequencing metadata and sharing via the GISAID initiative. We would like to thank all the volunteers for devoting their time to our research. We thank members of the Core Facility of Microbiology and Parasitology (SHMC) of Fudan University for their

636 continuous support. The analysis of bulk and single-cell RNA sequencing data was
637 supported by the Medical Science Data Center in Shanghai Medical College of Fudan
638 University.

639

640 **Funding** The National Key Research and Development Program (2021YFA1301404 and
641 2023YFC0872600). The National Natural Science Foundation of China (32370943), and
642 the Shanghai Municipal Science and Technology Major Project (ZD2021CY001). The
643 Non-profit Central Research Institute Fund of the Chinese Academy of Medical Sciences
644 (2023-PT310-02 to Q.W.).

645

## References

1. Lu LL, Suscovich TJ, Fortune SM, Alter G. Beyond binding: antibody effector functions in infectious diseases. *Nat Rev Immunol*. 2018;18(1):46–61.
2. Burton DR. Antiviral neutralizing antibodies: from in vitro to in vivo activity. *Nat Rev Immunol*. 2023;23(11):720–34.
3. Wells TJ, Esposito T, Henderson IR, Labzin LI. Mechanisms of antibody-dependent enhancement of infectious disease. *Nat Rev Immunol*. 2025;25(1):6–21.
4. Lee WS, Wheatley AK, Kent SJ, DeKosky BJ. Antibody-dependent enhancement and SARS-CoV-2 vaccines and therapies. *Nat Microbiol*. 2020;5(10):1185–91.
5. Jaume M, Yip MS, Cheung CY, Leung HL, Li PH, Kien F, et al. Anti-severe acute respiratory syndrome coronavirus spike antibodies trigger infection of human immune cells via a pH- and cysteine protease-independent FcgammaR pathway. *J Virol*. 2011;85(20):10582–97.
6. Yip MS, Leung NH, Cheung CY, Li PH, Lee HH, Daeron M, et al. Antibody-dependent infection of human macrophages by severe acute respiratory syndrome coronavirus. *Virol J*. 2014;11:82.
7. Wan Y, Shang J, Sun S, Tai W, Chen J, Geng Q, et al. Molecular Mechanism for Antibody-Dependent Enhancement of Coronavirus Entry. *J Virol*. 2020;94(5).
8. Arvin AM, Fink K, Schmid MA, Cathcart A, Spreafico R, Havenar-Daughton C, et al. A perspective on potential antibody-dependent enhancement of SARS-CoV-2. *Nature*. 2020;584(7821):353–63.
9. Iwasaki A, Yang Y. The potential danger of suboptimal antibody responses in COVID-19. *Nat Rev Immunol*. 2020;20(6):339–41.
10. Zhou Y, Liu Z, Li S, Xu W, Zhang Q, Silva IT, et al. Enhancement versus neutralization by SARS-CoV-2 antibodies from a convalescent donor associates with distinct epitopes on the RBD. *Cell Rep*. 2021;34(5):108699.
11. Wang S, Wang J, Yu X, Jiang W, Chen S, Wang R, et al. Antibody-dependent enhancement (ADE) of SARS-CoV-2 pseudoviral infection requires FcgammaRIIB and virus-antibody complex with bivalent interaction. *Commun Biol*. 2022;5(1):262.
12. Li D, Edwards RJ, Manne K, Martinez DR, Schafer A, Alam SM, et al. In vitro and in vivo functions of SARS-CoV-2 infection-enhancing and neutralizing antibodies. *Cell*. 2021;184(16):4203–19 e32.
13. Shen XR, Li Q, Li HL, Wang X, Wang Q, Zheng XS, et al. Antibody-Dependent Enhancement of SARS-CoV-2 Infection of Human Immune Cells: In Vitro Assessment Provides Insight in COVID-19 Pathogenesis. *Viruses*. 2021;13(12).
14. Maemura T, Kuroda M, Armbrust T, Yamayoshi S, Halfmann PJ, Kawaoka Y. Antibody-Dependent Enhancement of SARS-CoV-2 Infection Is Mediated by the IgG Receptors FcgammaRIIA and FcgammaRIIIA but Does Not Contribute to Aberrant Cytokine Production by Macrophages. *mBio*. 2021;12(5):e0198721.
15. Houser KV, Broadbent AJ, Gretebeck L, Vogel L, Lamirande EW, Sutton T, et al. Enhanced inflammation in New Zealand white rabbits when MERS-CoV reinfection occurs in the absence of neutralizing antibody. *PLoS Pathog*. 2017;13(8):e1006565.
16. Tseng CT, Sbrana E, Iwata-Yoshikawa N, Newman PC, Garron T, Atmar RL, et al. Immunization with SARS coronavirus vaccines leads to pulmonary immunopathology on challenge with the SARS virus. *PLoS*

*One*. 2012;7(4):e35421.

17. Holmes EC. The Emergence and Evolution of SARS-CoV-2. *Annu Rev Virol*. 2024;11(1):21–42.

18. Ma W, Fu H, Jian F, Cao Y, Li M. Immune evasion and ACE2 binding affinity contribute to SARS-CoV-2 evolution. *Nat Ecol Evol*. 2023;7(9):1457–66.

19. Xue S, Han Y, Wu F, Wang Q. Mutations in the SARS-CoV-2 spike receptor binding domain and their delicate balance between ACE2 affinity and antibody evasion. *Protein Cell*. 2024;15(6):403–18.

20. Zhang J, Zhang Y, Kang JY, Chen S, He Y, Han B, et al. Potential transmission chains of variant B.1.1.7 and co-mutations of SARS-CoV-2. *Cell Discov*. 2021;7(1):44.

21. Wu J, Chen Z, Gao Y, Wang Z, Wang J, Chiang BY, et al. Fortuitous somatic mutations during antibody evolution endow broad neutralization against SARS-CoV-2 Omicron variants. *Cell Rep*. 2023;42(5):112503.

22. Xia S, Jiao F, Chen J, Wang L, Lu T, Wang Q, et al. MERS-related coronavirus circulating in pangolins exhibits strong fusogenicity in human cells and high sensitivity to fusion inhibitors. *Cell Rep Med*. 2025:102277.

23. Zhang H, Shi S, Sun L, Li S, Zhang Y, Li Z, et al. Screening and discovery of an antiviral candidate inhibiting the SARS-CoV-2 envelope (2-E) channel. *Curr Res Microb Sci*. 2025;9:100409.

24. Jiang W, Wu J, He J, Xia A, Wu W, Gao Y, et al. Re-Evaluation and Retrospective Comparison of Serum Neutralization Induced by Three Different Types of Inactivated SARS-CoV-2 Vaccines. *Vaccines (Basel)*. 2024;12(11).

25. Liu Z, Zhou J, Wang W, Zhang G, Xing L, Zhang K, et al. Neutralization of SARS-CoV-2 BA.2.86 and JN.1 by CF501 adjuvant-enhanced immune responses targeting the conserved epitopes in ancestral RBD. *Cell Rep Med*. 2024;5(3):101445.

26. Shaymardanov AM, Antonova OA, Sokol AD, Deinichenko KA, Kazakova PG, Milovanov MM, et al. Single-Cell Gene Expression Analysis Revealed Immune Cell Signatures of Delta COVID-19. *Cells*. 2022;11(19).

27. Wang H, Liu C, Xie X, Niu M, Wang Y, Cheng X, et al. Multi-omics blood atlas reveals unique features of immune and platelet responses to SARS-CoV-2 Omicron breakthrough infection. *Immunity*. 2023;56(6):1410–28 e8.

28. Ren X, Wen W, Fan X, Hou W, Su B, Cai P, et al. COVID-19 immune features revealed by a large-scale single-cell transcriptome atlas. *Cell*. 2021;184(7):1895–913 e19.

29. Wang K, Jia Z, Bao L, Wang L, Cao L, Chi H, et al. Memory B cell repertoire from triple vaccinees against diverse SARS-CoV-2 variants. *Nature*. 2022;603(7903):919–25.

30. Peng X, Han Y, Xue S, Zhou Y, Jiang W, Xia A, et al. Low Antibody-Dependent Enhancement of Viral Entry Activity Supports the Safety of Inactivated SARS-CoV-2 Vaccines. *Vaccines (Basel)*. 2025;13(4).

31. Bianchini F, Crivelli V, Abernathy ME, Guerra C, Palus M, Muri J, et al. Human neutralizing antibodies to cold linear epitopes and subdomain 1 of the SARS-CoV-2 spike glycoprotein. *Sci Immunol*. 2023;8(81):eade0958.

32. Afzali B, Noris M, Lambrecht BN, Kemper C. The state of complement in COVID-19. *Nat Rev Immunol*. 2022;22(2):77–84.

33. Okuya K, Hattori T, Saito T, Takadate Y, Sasaki M, Furuyama W, et al. Multiple Routes of Antibody-Dependent Enhancement of SARS-CoV-2 Infection. *Microbiol Spectr*. 2022;10(2):e0155321.

34. Bonaventura A, Vecchie A, Dagna L, Martinod K, Dixon DL, Van Tassell BW, et al. Endothelial

727 dysfunction and immunothrombosis as key pathogenic mechanisms in COVID-19. *Nat Rev Immunol*.
728 2021;21(5):319–29.
729 35. Manne BK, Denorme F, Middleton EA, Portier I, Rowley JW, Stubben C, et al. Platelet gene expression
730 and function in patients with COVID-19. *Blood*. 2020;136(11):1317–29.
731 36. Sheikh A, McMenamin J, Taylor B, Robertson C, Public Health S, the EIIC. SARS-CoV-2 Delta VOC
732 in Scotland: demographics, risk of hospital admission, and vaccine effectiveness. *Lancet*.
733 2021;397(10293):2461–2.
734 37. Ong SWX, Chiew CJ, Ang LW, Mak TM, Cui L, Toh M, et al. Clinical and Virological Features of
735 Severe Acute Respiratory Syndrome Coronavirus 2 (SARS-CoV-2) Variants of Concern: A Retrospective
736 Cohort Study Comparing B.1.1.7 (Alpha), B.1.351 (Beta), and B.1.617.2 (Delta). *Clin Infect Dis*.
737 2022;75(1):e1128–e36.
738 38. Li B, Deng A, Li K, Hu Y, Li Z, Shi Y, et al. Viral infection and transmission in a large, well-traced
739 outbreak caused by the SARS-CoV-2 Delta variant. *Nat Commun*. 2022;13(1):460.
740 39. Mlcochova P, Kemp SA, Dhar MS, Papa G, Meng B, Ferreira I, et al. SARS-CoV-2 B.1.617.2 Delta
741 variant replication and immune evasion. *Nature*. 2021;599(7883):114–9.
742 40. Zhang J, Xiao T, Cai Y, Lavine CL, Peng H, Zhu H, et al. Membrane fusion and immune evasion by the
743 spike protein of SARS-CoV-2 Delta variant. *Science*. 2021;374(6573):1353–60.
744 41. Junqueira C, Crespo A, Ranjbar S, de Lacerda LB, Lewandrowski M, Ingber J, et al. FcgammaR-
745 mediated SARS-CoV-2 infection of monocytes activates inflammation. *Nature*. 2022;606(7914):576–84.
746 42. Henry BM, Szergyuk I, de Oliveira MHS, Lippi G, Benoit JL, Vikse J, et al. Complement levels at
747 admission as a reflection of coronavirus disease 2019 (COVID-19) severity state. *J Med Virol*.
748 2021;93(9):5515–22.
749 43. Sefik E, Qu R, Junqueira C, Kaffe E, Mirza H, Zhao J, et al. Inflammasome activation in infected
750 macrophages drives COVID-19 pathology. *Nature*. 2022;606(7914):585–93.
751 44. Merad M, Martin JC. Pathological inflammation in patients with COVID-19: a key role for monocytes
752 and macrophages. *Nat Rev Immunol*. 2020;20(6):355–62.
753 45. Moulana A, Dupic T, Phillips AM, Chang J, Nieves S, Roffler AA, et al. Compensatory epistasis
754 maintains ACE2 affinity in SARS-CoV-2 Omicron BA.1. *Nat Commun*. 2022;13(1):7011.
755 46. Starr TN, Greaney AJ, Hannon WW, Loes AN, Hauser K, Dillen JR, et al. Shifting mutational
756 constraints in the SARS-CoV-2 receptor-binding domain during viral evolution. *Science*.
757 2022;377(6604):420–4.
758 47. Renner M, Flanagan A, Dejnirattisai W, Puttikhunt C, Kasinrerk W, Supasa P, et al. Characterization of
759 a potent and highly unusual minimally enhancing antibody directed against dengue virus. *Nat Immunol*.
760 2018;19(11):1248–56.
761 48. Gu C, Cao X, Wang Z, Hu X, Yao Y, Zhou Y, et al. A human antibody of potent efficacy against SARS-
762 CoV-2 in rhesus macaques showed strong blocking activity to B.1.351. *MAbs*. 2021;13(1):1930636.
763

# Figures and Figure Legends

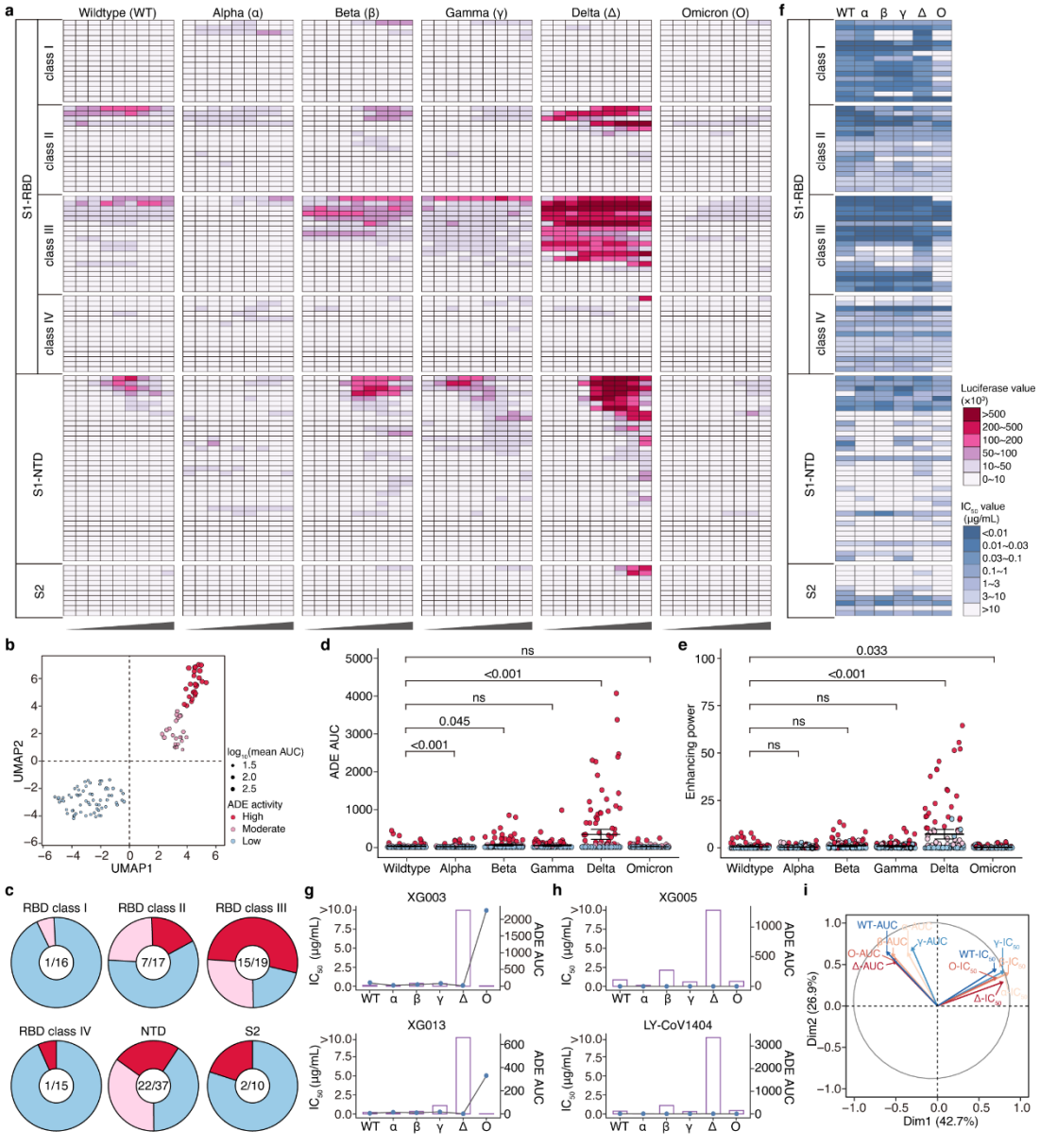


**Fig. 1: Enhanced ADE activity in Delta variant associates with S epitope specificity rather than neutralization efficiency.**

(**a**) Heatmap depicting in vitro ADE activity of 114 mAbs across pseudotyped SARS-CoV-2 variants. Each mAb (rows) was tested at nine-point three-fold dilutions (columns) starting from 100 μg/mL. Relative luminescence intensity reflects viral entry efficiency, with gradient colors indicating ADE magnitude. Representative of at least two experiments.

(**b**) UMAP projection of mAb ADE AUC profiles across variants, revealing three distinct clusters: high (red), moderate (pink), and low (blue) ADE activity.

(**c**) Distribution of ADE activity among mAbs grouped by epitope. Each pie chart represents a distinct group

of mAbs recognizing the same epitope: RBD class I/II/III/IV, NTD, and S2 region. Within each pie, the colored slices indicate the proportion of mAbs exhibiting high (red), moderate (pink), and low (blue) ADE activity.

(**d-e**) Comparative ADE AUC (**d**) and enhancing power (**e**) across VOCs relative to wildtype. Each dot represents a mAb. Statistical significance analyzed using Kruskal-Wallis test with Dunnett's multiple comparisons and corrected with Benjamini-Hochberg corrected. ns, not statistically significant.

(**f**) Neutralization potency ($IC_{50}$) of mAbs across SARS-CoV-2 variants. Experiments were repeated at least three times.

(**g-h**) ADE AUC (bar) and $IC_{50}$ (dot and line) values across VOCs for mAbs XG003 and XG013 (**g**), and XG005 and LY-CoV1404 (**h**).

(**i**) Principal component analysis (PCA) of mAb profiles showing dissociation between ADE AUC and $IC_{50}$ dimensions.

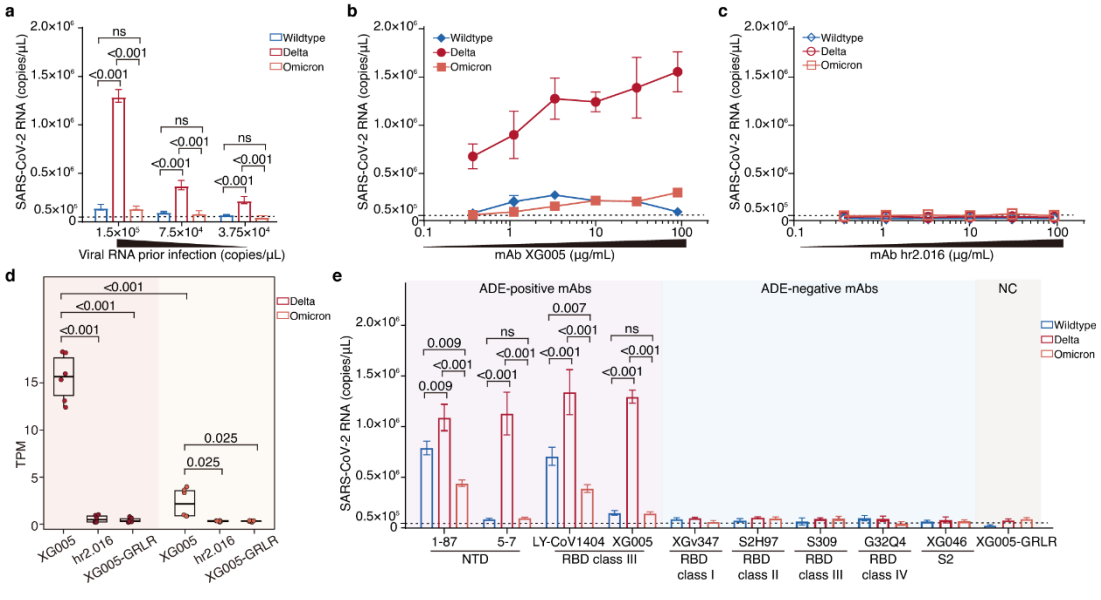


**Fig. 2: Authentic Delta variant exhibited potent ADE-mediated viral entry compared with wildtype and Omicron.**

(**a**) ADE activity of mAb XG005 [21] against authentic SARS-CoV-2 variants at three viral loads ($1{\cdot}50\times10^5$, $7{\cdot}50\times10^4$, and $3{\cdot}75\times10^4$ RNA copies/μL). Data represent mean ± SD of at least three technical replicates.

(**b-c**) Concentration-dependent ADE activity of ADE-positive mAb XG005 (**b**) and ADE-negative mAb hr2.016 [31] (**c**) against authentic variants ($1{\cdot}50\times10^5$ RNA copies/μL). Data represent mean ± SD of at least three replicates.

(**d**) Viral genome quantification (transcripts per million, TPM) via bulk RNA-seq in Raji cells infected with authentic Delta/Omicron variants in the presence of indicated mAbs. Box plots show the median (center line), interquartile range (box limits), and minimum and maximum range (whiskers). XG005-GRLR, FcγR-binding deficient mutant.

(**e**) ADE activity of epitope-specific mAbs against authentic variants. XG005-GRLR served as negative control (NC). The experiments were performed with three technical replicates. Data show mean ± SD of at least three replicates.

(**a, d and e**) Statistical comparisons using Kruskal-Wallis test with Dunnett's multiple comparisons and corrected with Benjamini-Hochberg adjustment for *p* values. ns, not statistically significant.

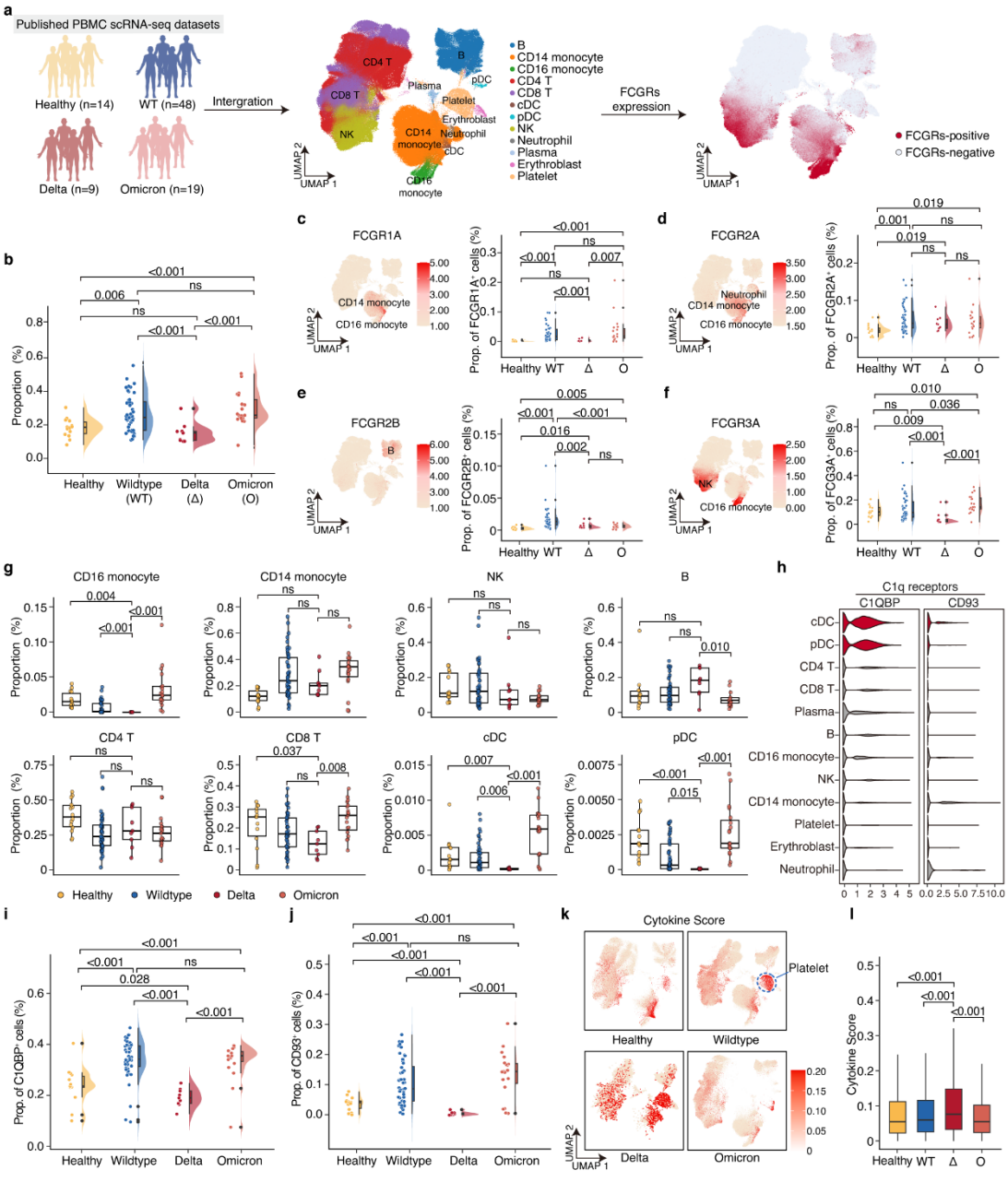


**Fig. 3: Depletion of FcγR⁺ and C1qR⁺ immune cells in Delta-infected patients.**

(**a**) Study design. Integrated scRNA-seq analysis of PBMCs from healthy controls (n = 14, yellow) and patients infected with wildtype (WT, n = 48, blue), Delta (n = 9, crimson), or Omicron (n = 19, orange) SARS-CoV-2 (left). UMAP projection (middle) shows 12 annotated cell clusters, with further analysis focused on FcγR⁺ cells (right).

(**b**) Proportion of FcγR⁺ cells (expressing ≥1 FCGR genes) across cohorts. Each dot represents a donor.

(**c-f**) UMAP visualization of FCGR1A⁺ (**c**), FCGR2A⁺ (**d**), FCGR2B⁺ (**e**), and FCGR3A⁺ (**f**) cells. Bar graphs show subtype proportions within total FcγR-expressing cells compartment.

(**g**) Compositional changes in major immune cell populations across cohorts. Each dot represents an individual or a patient.

(**h**) Violin plots of C1qR (C1QBP and CD93) expression across PBMC subsets.

(**i-j**) Proportion of $C1QBP^+$ (**i**), and $CD93^+$ (**j**) cells within total $C1qR^+$ compartment.

(**k**) UMAP visualization of cytokine scores (derived from 75-gene panel).

(**l**) Quantitative cytokine scores across cohorts.

(**b-g, i-j, and l**) Statistical analyses assessed by Kruskal-Wallis test with Dunnett's multiple comparisons and corrected with Benjamini-Hochberg adjustment. ns, not statistically significant.

(**g and l**) Box plots show the median (center line), interquartile range (box limits), and minimum and maximum range (whiskers).

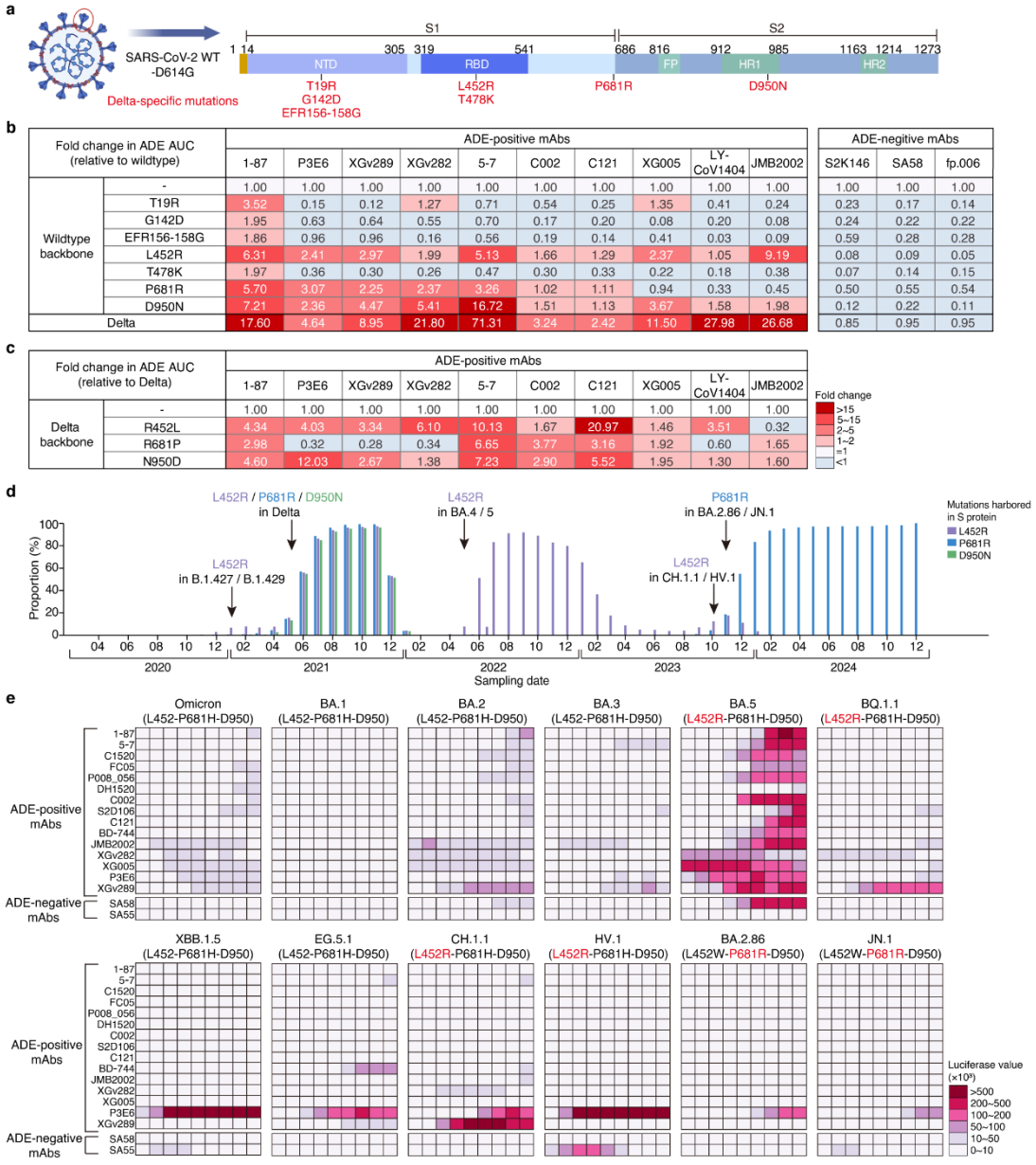


**Fig. 4: Epistatic interactions within the S protein govern ADE capacity.**

(**a**) Delta-specific S mutations versus SARS-CoV-2 wildtype (WT) and other VOCs.

(**b**) ADE AUC fold change (relative to wildtype) for pseudoviruses with single point mutations in wildtype backbone. Data represent mean of at least two technical replicates.

(**c**) ADE AUC fold change (relative to Delta) for pseudoviruses with reversion mutations in Delta backbone. Data show mean of at least two technical replicates.

(**d**) Global prevalence dynamics of L452R/P681R/D950N-harboring variants. Bar represents percentage of variant sequences harboring indicated mutations per month (y axis) from January, 2020 to December, 2024 (x axis).

(**e**) Heatmap depicting in vitro ADE activity of ADE-positive (n = 15) and ADE-negative (n = 2) mAbs against

837 Omicron sub-lineages. Each mAb (rows) was tested at nine-point three-fold dilutions (columns) starting from
838 100 μg/mL. Relative luminescence intensity reflects viral entry efficiency, with gradient colors indicating
839 ADE magnitude. Experiments were repeated at least two times.
840

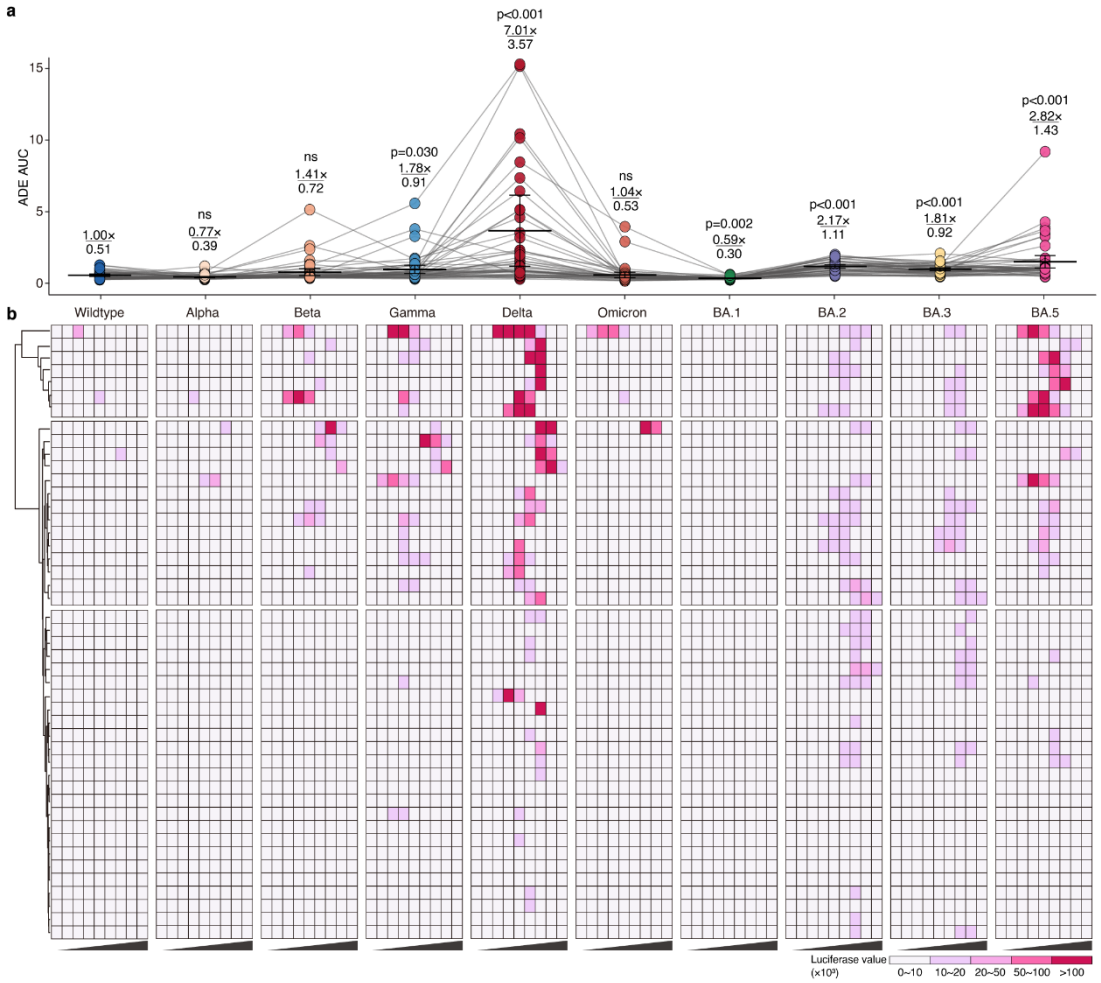


**Fig. 5: Variant-dependent heterogeneity in ADE mediated by serum samples.**

(**a**) Comparative ADE AUC (y axis) of donors' sera (n = 46) against VOCs and Omicron sub-lineages relative to wildtype. Each dot represents one serum sample. Fold change relative to wildtype for each variant shown above the line; mean value displayed below the line. Statistical analysis assessed by Kruskal-Wallis test with Dunnett's multiple comparisons and corrected with Benjamini-Hochberg adjustment. ns, not statistically significant.

(**b**) Heatmap of serological ADE activity across SARS-CoV-2 variants. Each serum sample (rows) was tested against pseudotyped viruses at nine-point three-fold serial dilutions (columns) starting from 1:4 serum dilution. Sera were collected from vaccinated or convalescent individuals (n = 46). Relative luminescence intensity reflects viral entry efficiency, with gradient colors indicating ADE magnitude. Representative of two replicates.

# Supplementary Information

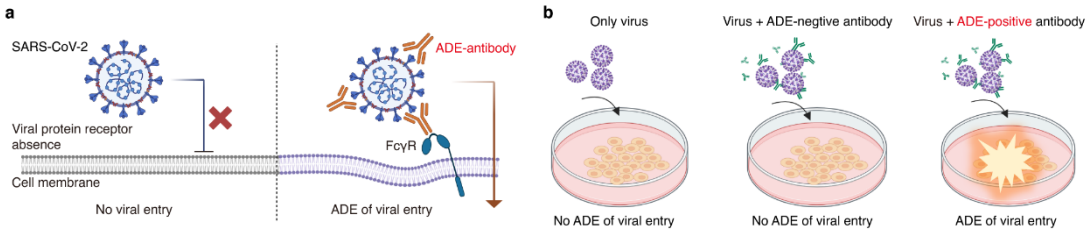


**Supplementary Fig. S1: Mechanisms of ADE of viral entry.**

(**a**) Schematic of ADE of viral entry mediated by FcγRs. Antibody Fab fragments bind SARS-CoV-2 S proteins while Fc regions engage FcγRs on immune cells, facilitating viral entry.

(**b**) In vitro pseudovirus ADE assay design. Raji cells expressing FcγRIIB (lacking host receptor ACE2) serve as target cells. S-expressing pseudoviruses encoding luciferase reporter require ADE-positive antibodies for FcγR-mediated entry and subsequent luciferase expression. Viral entry is quantified by measuring luciferase activity.

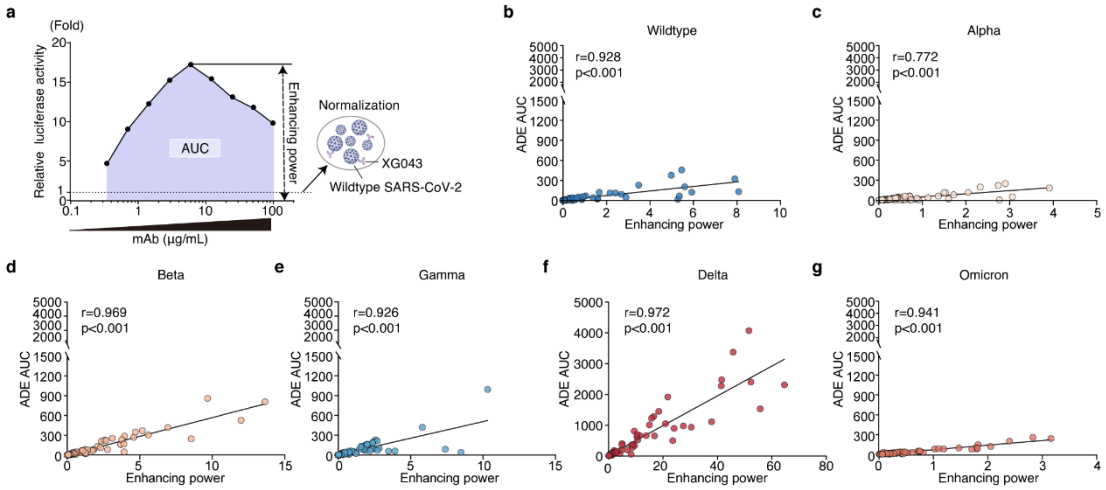


**Supplementary Fig. S2: Quantitative metrics for ADE activity.**

(**a**) Schematic illustrating two ADE quantification parameters. ADE area under curve (ADE AUC) integrates concentration-dependent enhancement, while ADE enhancing power represents maximum viral entry efficiency across antibody dilutions.

(**b-g**) Correlation between ADE AUC and enhancing power for all mAbs against SARS-CoV-2 variants, including wildtype (**b**), Alpha (**c**), Beta (**d**), Gamma (**e**), Delta (**f**), and Omicron (**g**). Each dot represents individual mAbs (n = 114). Solid lines show linear regression fits, with statistics calculated using Spearman's rank correlation method.

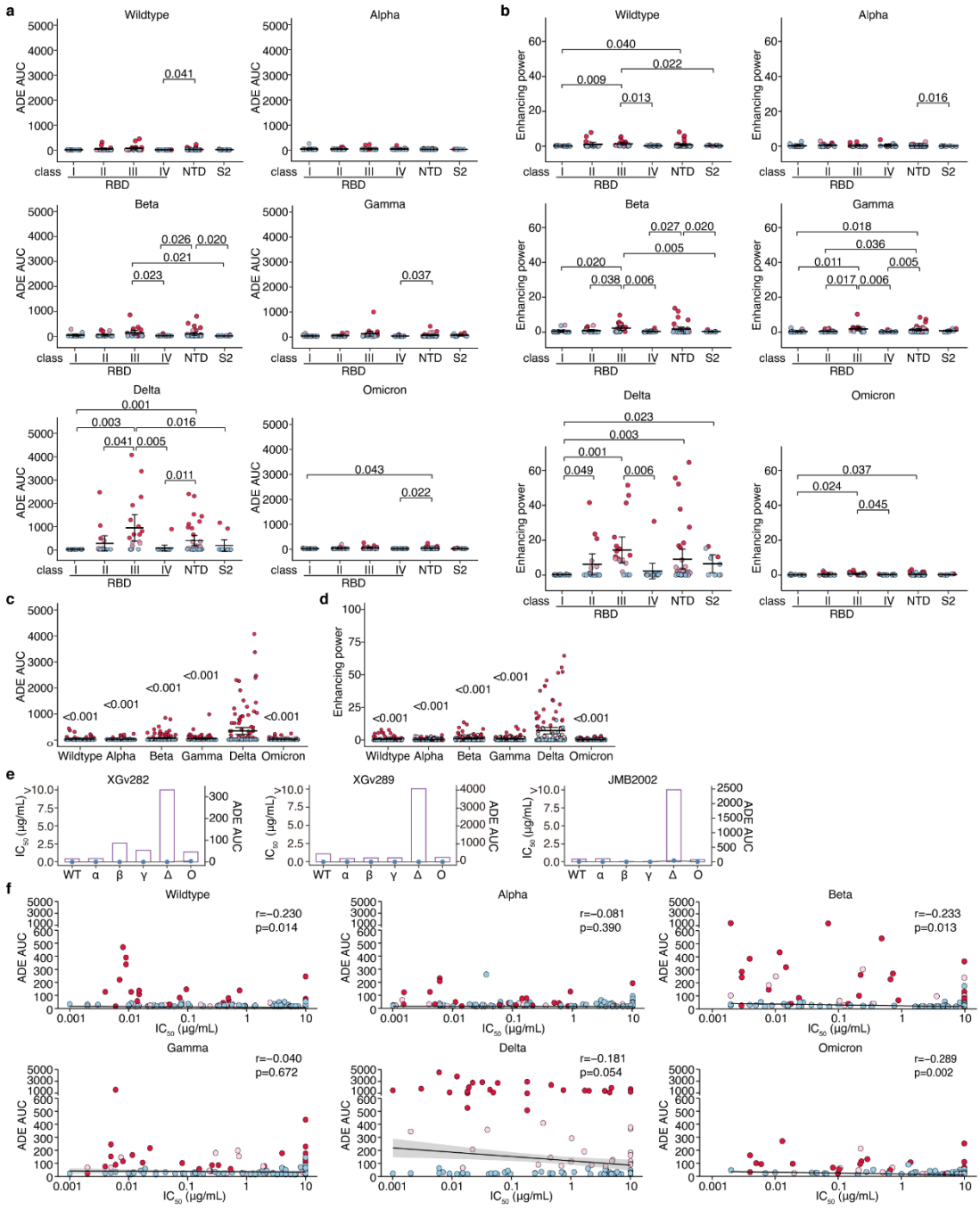


**Supplementary Fig. S3. Enhanced ADE in Delta variant associated with S epitopes rather than neutralizing efficiency.**

(**a-b**) Comparative ADE AUC (**a**) and enhancing power (**b**) of mAbs grouped by S epitope specificity across SARS-CoV-2 variants. Each dot represents a mAb. Data show mean ± SD of at least two technical replicates.

(**c-d**) ADE AUC (**c**) and enhancing power (**d**) for wildtype and VOCs relative to Delta. Each dot represents a mAb. Data show mean ± SD.

(**e**) ADE AUC (bar) and $IC_{50}$ (dot and line) values across VOCs for mAbs XGv282[29], XGv289[29], and JMB2002[48].

(**f**) Correlation analyses of ADE AUC versus $IC_{50}$ values for all mAbs across SARS-CoV-2 variants. Each dot represents an individual mAbs (n = 114). Solid lines show linear regression fits. Statistics calculated using Spearman's rank correlation method.

(**a-d**) Statistical analyses assessed using Kruskal-Wallis test with Dunnett's multiple comparisons and corrected with Benjamini-Hochberg adjustment.

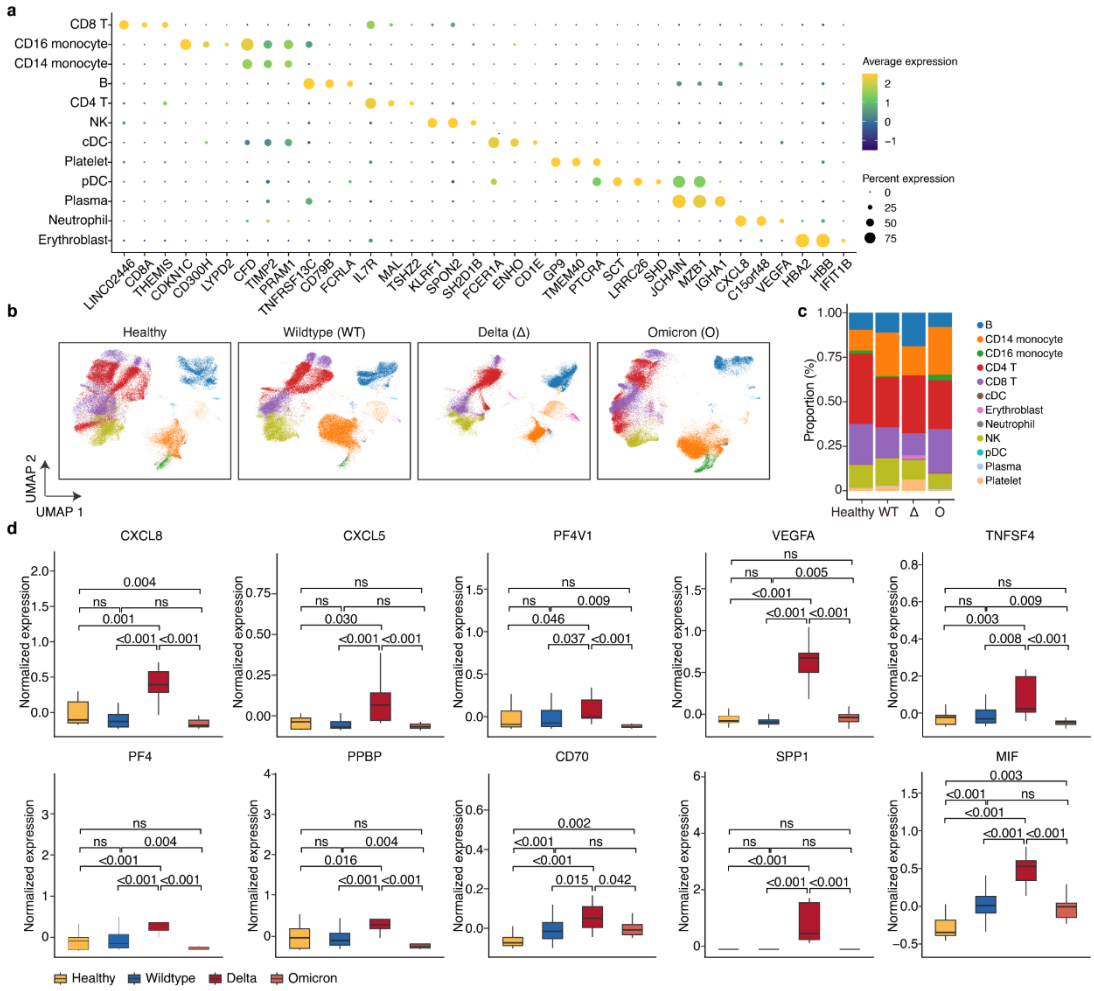


**Supplementary Fig. S4: Integrated scRNA-seq analysis of PBMCs from SARS-CoV-2-infected patients and healthy controls.**

(**a**) Expression distribution of canonical markers defining major PBMC populations (rows) across key genes (columns).

(**b**) UMAP projection of single PBMCs from healthy controls (n = 14) and patients infected with wildtype SARS-CoV-2 (n = 48), Delta (n = 9), or Omicron (n = 19). Each dot represents a single cell colored by annotated cell types.

(**c**) Compositional analysis of immune cell subsets across cohorts. Stacked bars show average proportions.

(**d**) Cytokine gene expression across cohorts. Box plots show the median (center line), interquartile range (box limits), and minimum and maximum range (whiskers). Statistical analyses calculated using Kruskal-Wallis test with Dunnett's multiple comparisons and corrected with Benjamini-Hochberg adjustment.

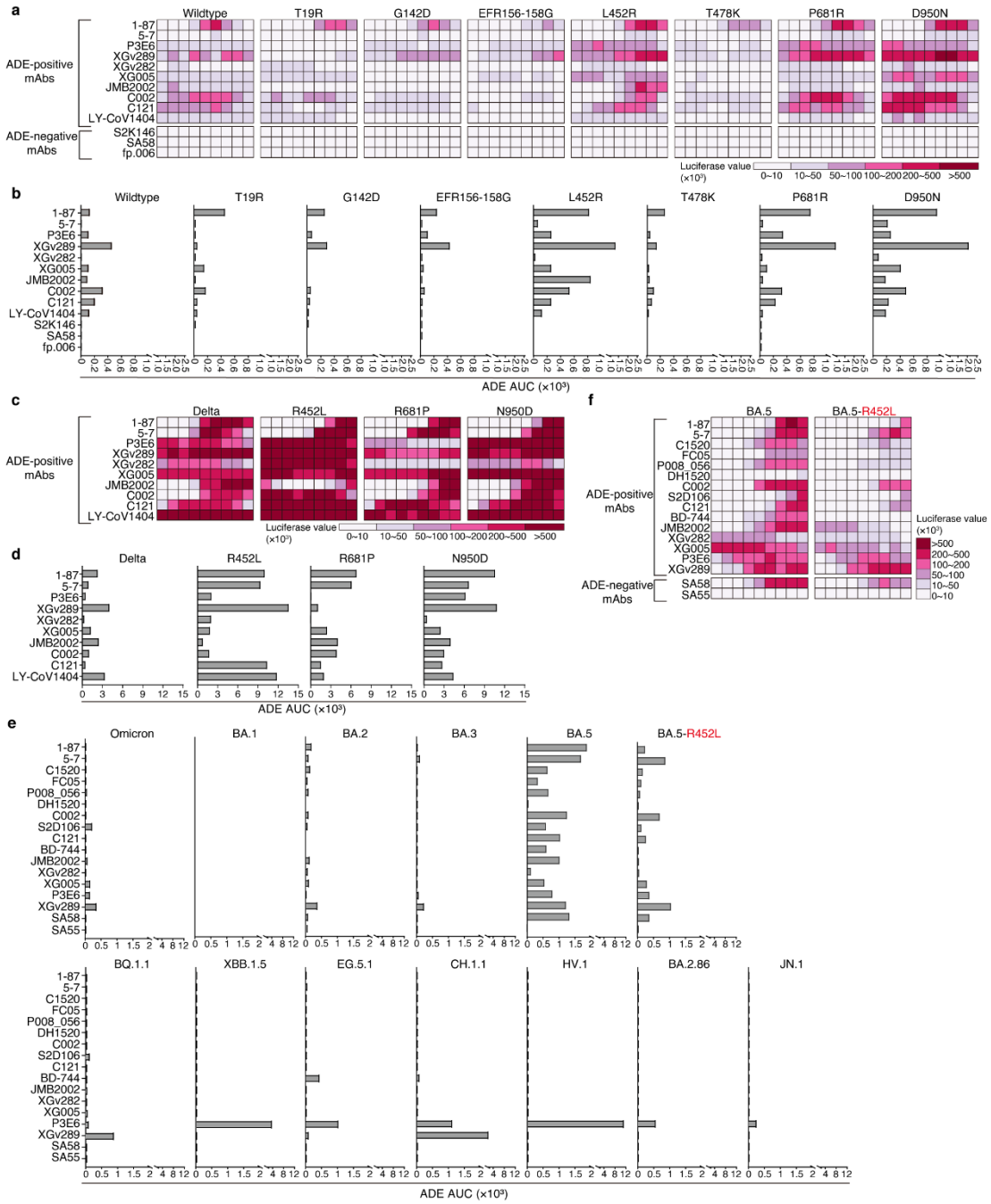


**Supplementary Fig. S5: ADE activity against across diverse S mutants.**

(**a, c and f**) Heatmap depicting in vitro ADE activity against the wildtype SARS-CoV-2 and its related point-mutant pseudoviruses (**a**), the Delta variant and its related point-mutant pseudoviruses (**c**), and the BA.5 and BA.5-R452L mutant pseudoviruses (**f**). Each mAb (rows) was tested at nine-point three-fold dilutions (columns) starting from 100 μg/mL. Relative luminescence intensity reflects viral entry efficiency, with gradient colors indicating ADE magnitude. Experiments were repeated at least two times.

(**b, d and e**) ADE AUC quantitation for mAbs against the wildtype SARS-CoV-2 and its related point-mutant pseudoviruses (**b**), the Delta variant and its related point-mutant pseudoviruses (**d**), and the Omicron variant

911 and its sub-lineages, as well as BA.5-R452L mutant (**e**).

912

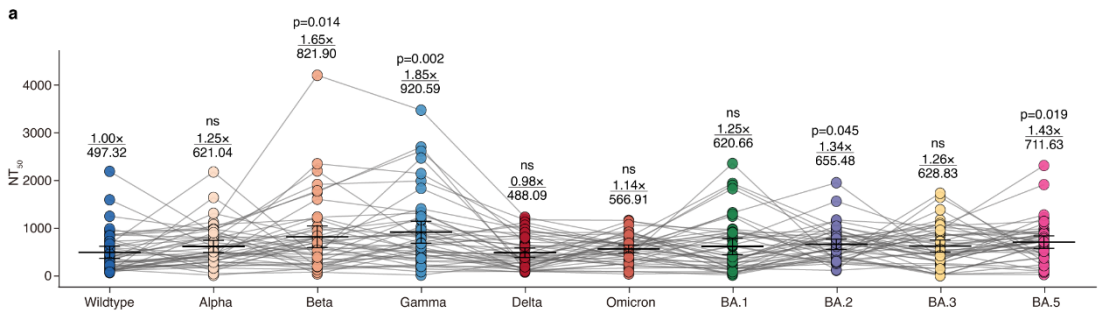


**Supplementary Fig. S6: Serological neutralization potency against SARS-CoV-2 variants.**
(**a**) Comparative neutralizing titers ($NT_{50}$) of donors' sera across SARS-CoV-2 variants. Each dot represents a serum sample (n = 46). Data are presented as mean ± SD of two technical replicates. Fold change relative to wildtype for each variant shown above the line; mean value displayed below the line. Statistical analysis calculated by Kruskal-Wallis with Dunnett's multiple comparisons and corrected with Benjamini-Hochberg adjustment. ns, not statistically significant.

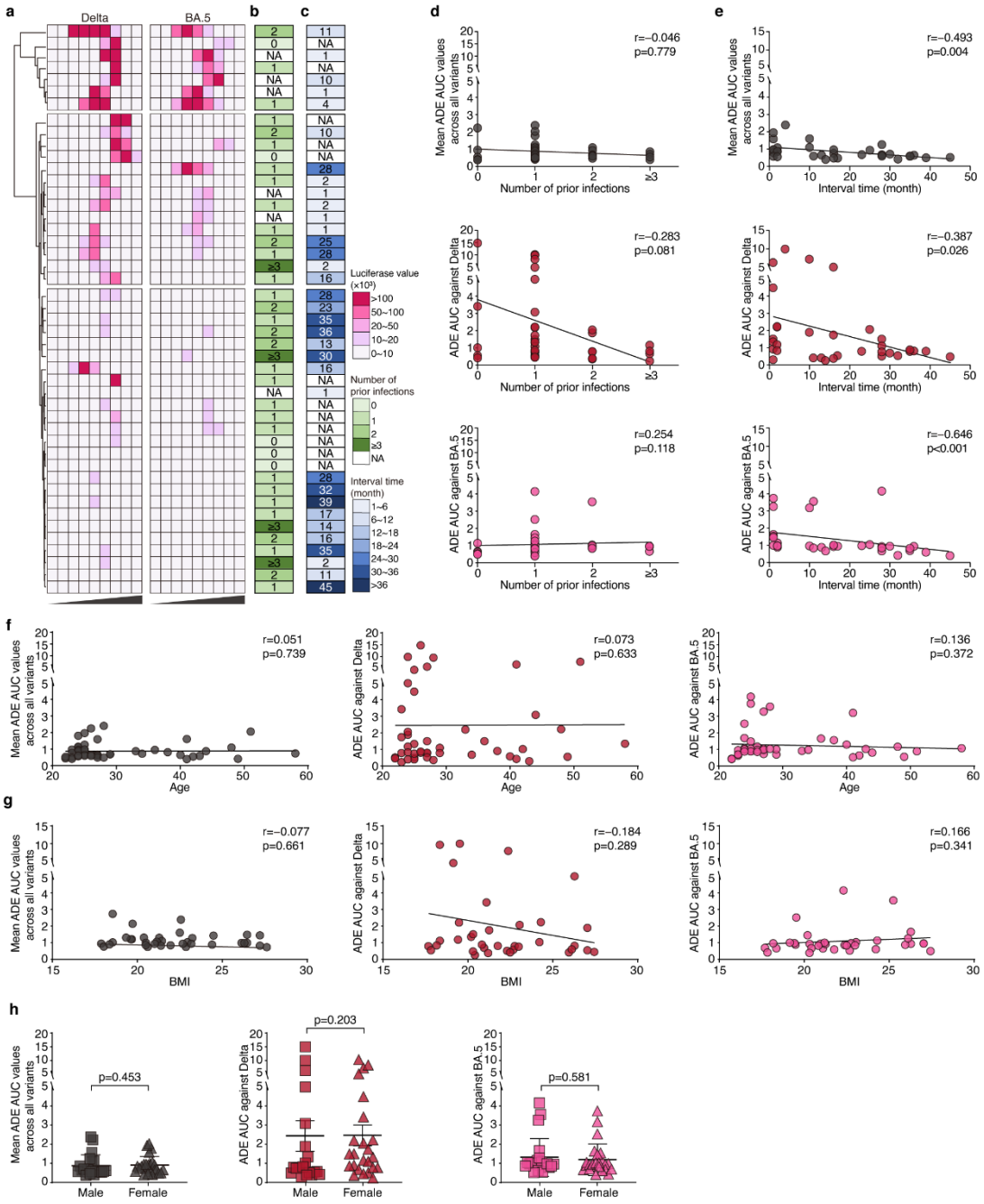


**Supplementary Fig. S7: Correlation analyses between volunteers' characteristics and serological ADE AUC.**

(**a-c**) Characterization of donors' sera. Heatmap depicting in vitro ADE activity against the Delta and BA.5 variants (**a**), the number of prior SARS-CoV-2 infections (**b**), and interval time from COVID-19 recovery to blood sampling (**c**). NA, not available.

(**d-g**) Correlation analyses of ADE AUC versus the number of prior SARS-CoV-2 infections (**d**; n = 40), recovering-to-sampling interval (**e**; n = 34), volunteers' age (**f**; n = 46), and volunteers' body mass index (BMI) (**g**; n = 36). Each dot represents a serum sample. Solid lines show linear regression fits. Statistics calculated

using Spearman's rank correlation method.

(**h**) Comparative analyses of ADE AUC between male and female donors. Statistical analyses calculated using Mann-Whitney test.

**Supplementary Table S1. Comprehensive mAb panel for in vitro ADE profiling.**
Summary of 114 human mAbs used in ADE assays, including 35 XG mAbs, 41 XGv mAbs and 38 structurally characterized mAbs.

**Supplementary Table S2. Functional characterization of anti-S mAbs.**
Binding affinity ($EC_{50}$) and neutralization potency ($IC_{50}$ against SARS-CoV-2 variants) for all tested mAbs.

**Supplementary Table S3. Differential cytokine gene expression in vivo across SARS-CoV-2 variants.**
A curated panel of 75 cytokine-related genes analyzed by scRNA-seq, with mean expression levels and differential expression statistics across cohorts, including wildtype, Delta, and Omicron infections, as well as healthy controls.

**Supplementary Table S4. Demographic and clinical characteristics of serum donors**
Summary of 46 SARS-CoV-2-recovered volunteers including age, gender, vaccination status, number of prior infections, and sample collection timeline relative to diagnosis.